Micro-computed tomography imaging and probabilistic modelling of rock fracture by freeze–thaw

Article (Accepted Version)

Micro-computed tomography imaging and probabilistic modelling of rock fracture by freeze–thaw

Vikram Maji[1] and Julian B. Murton[2]

Permafrost Laboratory, Department of Geography, University of Sussex, Brighton BN1 9QJ, UK

[1] Corresponding author; v.maji@sussex.ac.uk

[2] j.b.murton@sussex.ac.uk

Abstract

A major problem in studies of rock fracture by frost is the paucity of direct observations in space and time of the initiation and growth of microcracks and their transition to macrocracks. Such observations are essential to understand the location, timing and controls of rock fracture by freeze–thaw. The aim of the present work is to image and elucidate the early stages of rock fracture by applying imaging and statistical methods to a frost-weathering experiment using intact specimens of a limestone (chalk) and sandstone. First, micro-computed tomography (μ-CT) is used to visualise rock fracture in three dimensions over the course of 20 freeze–thaw cycles and to estimate transverse strain using a pixel-based approach. Second, probabilistic correlation functions are applied to quantify the progressive expansion of the fracture phase and associated damage to rock specimens. The method of μ-CT is demonstrated for visualising the growth and coalescence of microcracks and their transition to macrocracks. Fracture proceeded faster and to a greater extent in chalk relative to sandstone, and the macrocracks in chalk were mostly concentric and vertical. Both fracture development and positive transverse strain (dilation) accelerated after cycle 15, suggesting that a threshold has been exceeded, after which macrocracks were evident. Of three probabilistic correlation functions applied to the μ-CT results, the modified lineal-path function—which measures the continuous connectivity of the fracture phase in a specific

direction—reveals that damage was more extensive in the chalk than the sandstone. It also allows a novel approach to define and quantify three zones of microcracking during freeze–thaw cycling of anisotropic rock: (1) the *zone of inherent flaws*, (2) the *zone of active microcracking*, and (3) the *zone of weak influence during microcracking*. The broader significance of this work is that it provides a new approach to investigate mechanistically how frost action damages rock.

Keywords: Micro-CT; freeze–thaw; lineal-path function; plastic zone; probabilistic modelling; rock fracture

1. Introduction

The fracture of rock in cold regions by freeze–thaw processes influences the evolution of landscapes (Ballantyne, 2018) and the performance of engineering structures (Shiklomanov, Streletskiy, Grebenets, & Suter, 2017). Our understanding about the early stages of frost weathering of intact rock, however, is limited by a paucity of direct observations—in three dimensions (3-D) and through time—of the initiation and growth of microcracks and their evolution to macrocracks. A growing fracture can be considered using theoretical concepts from fracture mechanics of changes in the stress intensity factor in the plastic zone ahead of the crack tip of circular or elliptical holes (Griffith, 1921; Irwin, 1960; Mises, 1913; Dugdale, 1960; Vlahou, 2012, Vlahou & Worster, 2015) and modelled using the weighted-function or discrete-element methods. In the case of freezing-induced fractures, parameters such as fracture toughness, the size of inherent flaws and the degree of undercooling determine the extent of the plastic zone around the tip. Statistical modelling is required to define the dimensions of inherent flaws and the plastic zone as well as the probabilistic occurrences of multiple defects rather than single holes.

Here we report observations from laboratory testing on rock fracture and strain development during the early stages of frost weathering by monitoring intact sedimentary rock specimens at high resolution (35 μm) with micro-computed tomography (μ-CT). Micro-CT scanning is a powerful non-destructive method of imaging the internal morphology of objects based on the variable penetration of X-rays through material of differing density (Cnudde & Boone, 2013; Bultreys et. al., 2015). We apply three low-order probability functions (two-point, two-point cluster and lineal-path; Torquato, 1991 ; 2002) from materials science to repeated μ-CT scans of the same specimens to elucidate the development of the fracture phase and quantify the modal extent of inherent flaws and the plastic zone in two rock types of varying hardness (chalk and sandstone). From this, we determine the zones of inherent

flaws, intense microcracking and weak microcracking during freezing based on the probabilistic occurrence and extent of microcracks.

2. Material and Methods

2.1 Rock types and specimen preparation

A limestone and sandstone used in previous frost weathering experiments (Williams & Robinson, 2001; Murton, 2018) were selected. The limestone is Saint Cyr Tuffeau, a siliceous chalk that contains a large fraction of detrital quartz grains typically ~100 μm in diameter and set within a matrix of micrite and opal–cristobalite. The chalk is of Turonian (Upper Cretaceous) age and was collected from Lucet Quarry, Brézé-Saint-Cyren-Bourg, 10 km south of Saumur, France. The chalk shows freezing behaviour similar to frost-susceptible silt–clay, and is thought to experience microfracturing within a few freeze–thaw cycles (Murton, Peterson & Ozouf, 2006). It is relatively homogeneous but contains small fragments of fossils that can be used to orient specimens for repeated scanning and serve as markers to estimate strain. The sandstone is fine to medium-grained, poorly cemented and well laminated, from one of the two Masonry 'lifts' (beds) of the Ardingly Sandstone Member of the Tunbridge Wells Sand Formation (Radley & Allen, 2012). It is of Valanginian (Lower Cretaceous) age and was collected from Philpots Quarry, West Hoathly, West Sussex, UK. The density and uniaxial compressive strength of the sandstone (2130 kg m^{-3} and 72 MPa) are relatively high compared to those of the chalk (1350 kg m^{-3} and 0.53–9.24 MPa), whereas the porosity is lower (23–27% in sandstone vs. 47% in chalk, Murton et al., 2000; Williams & Robinson, 1981). Similar freezing conditions were tested on a soft frost-susceptible, relatively homogeneous chalk and a harder, non-frost-susceptible, heterogeneous sandstone.

Two cylindrical cores (30 mm long, 20 mm diameter)—one chalk, one sandstone—were obtained with a drill press, and their tops and bottoms flattened using an angular hand grinder. A cylindrical shape was selected to avoid acquisition artefacts arising from the variable penetration strength of X-rays within specimens with planar faces, because during a 360° scan X-rays must travel further along the direction diagonally inward from the corners of intersecting faces compared to the centre of each face. The small size of the specimens maximized the scanning resolution but was still of a size sufficient to simulate frost weathering in the outermost millimetres of rock (i.e., near-surface).

Prior to each freezing cycle, the specimens were wetted to facilitate frost weathering. A water table 5 mm above their base allowed them to saturate by capillary rise. Then, the rock cores were insulated beneath and around them with polystyrene to prevent lateral heat transfer during one-dimensional downward freezing. This freezing imposed a vertical thermal gradient. Natural winter and summer cycles were simulated at the Permafrost Laboratory of the University of Sussex, within an ECO 400 climate cabinet manufactured by Temperature Applied Science Ltd, UK. Twenty freeze–thaw cycles were carried out. For cycles 1–10 the temperature ranged from –5°C during freezing periods (24 hours) to 5°C during thawing periods (24 hours). For cycles 11 to 20, the temperature ranged from –10°C during freezing periods (5 days) to 10°C during thawing period (5 days). The increases in duration and temperature range were implemented to accelerate fracturing. The specimens were photographed before and after the experiment in order to identify macrofractures.

2.2 Micro-computed tomography (μ-CT)

Micro-CT scanning was undertaken with the Nikon Metrology XT H-225 tomography system in the Centre for Micromorphology at Queen Mary University, London. The system has an X-ray source, a rotating stage and an X-ray detector with 1000 x 1000 pixels. The source produces a cone-shaped X-ray beam—by bombarding a tungsten metal target with

electrons—that is focused on an object sitting on the rotating stage. The stage can rotate by 360° and the detector panel captures multiple two-dimensional (2-D) projections (radiographs) at 0.2° intervals. The radiographs show the amount of X-ray energy transmitted through the scanned object.

Before scanning, the system was auto-conditioned for several minutes to ensure a stable operating voltage. Then the specimen—encased in floral foam (to prevent movement during scanning)—was placed centrally on the rotating stage. A 360° test rotation was carried out to align the specimen centrally and ensure that the object fitted inside the field of view of the detector. The X, Y and Z coordinates of the stage relative to the x-ray source and detector were used during repeated scanning of the specimens (to eliminate spatial error). The acquisition parameters for each scan are listed in Table A.1. Penetration strength (and radiograph contrast) of the X-ray beam is mainly determined by the voltage, whereas the number of X-rays (and radiograph brightness) is determined largely by the current. The operation is based on a grey-scale histogram analysis to get the best range of grey-scale values between 9,000 and 60,000. Each scan of the entire specimen lasted ~3–4 hours, and the spatial resolution was 35 µm.

After scanning, the 2-D projections were aligned centrally in a radial pattern to reconstruct the 3-D volume. The pixels along each row of the detector became a slice. A cross section of the specimen was created from each row of pixels in the radiograph by using the method of back projection. A µ-CT reconstruction is thus a 3-D matrix in which each element consists of a voxel with a definite grey-scale value of 16 bits. The value is a function of the linear attenuation coefficient of the material scanned, which is a measure of the absorption and scattering of an X-ray beam passing through it. The value of the coefficient depends largely on the density and thickness of the material. The magnification of the object on the detector screen determines the size of the voxel. The reconstruction used *CT-Pro 3-D* software (Nikon

Metrology), which reassembled multiple 2-D projections into a 3-D volume. The operation generated a 16-bit TIFF image slice stack for further processing and visualisation. The development of the fracture phase within the specimens was visualised—at intervals during the course of the freeze-thaw cycling—using the rendering software *Drishti* (Australian National University, Australia). Details of the workflow for the μ-CT analysis are set out in Table A.2.

2.3 Transverse strain

Transverse strain of the rock specimens was measured using a pixel-based method in *Image J* software (U. S. National Institutes of Health, USA,), because the small size of the specimens and experimental set-up prevented use of miniature strain gauges. Strain was measured from 25 pairs of markers (e.g., fossil fragments, voids, grain boundaries and inherent structures) identified on horizontal slices at different depths in the upper, middle and lower parts of the chalk specimen in successive μ-CT images. Changes in the number of pixels between two identical marker pairs in repeated scans were measured to estimate progressive strain. Markers were selected on the circular cross sections perpendicular to the axial dimension to determine transverse strain. Axial strain was not measured because X-rays penetrate the upper and lower faces of the specimen at an oblique angle, whereas they enter the middle of it at a right angle (i.e., distortion increases from the middle towards the top and bottom of the specimens). As a result, each depth slice has same angle of X-ray penetration as the stage rotates by 360°, making it suitable for measuring transverse strain.

3. Theory

3.1 Background of fracture mechanics

Different textural inheritance in rocks leads to anisotropy in mechanical properties and therefore influences mechanisms of deformation and rock fracture (Hoagland, Hahn & Rosenfield, 1973). The pioneering theory of fracture mechanics developed by Griffiths (1921 & 1924) explained how the strain energy released during crack growth is used to develop fracture surfaces. Fracture growth in rocks is accompanied by inelastic deformation in the region ahead of crack tips. But the nature and characteristics of this region vary depending on the type of material. Metals commonly experience plasticity—which sometimes leads to strain hardening—and so the inelastic region ahead of crack tips in metals is named the *plastic zone*. Brittle materials, on the other hand, undergo microdamage due to the initiation of new microcracks and reactivation of existing ones, which commonly causes strain softening. As the inelastic region of brittle materials involves microfracturing, the region ahead of crack tips is called the fracture process zone (FPZ). Both regions dissipate substantial energy during fracturing, and the nature of the inelasticity determines the size and shape of the regions. In the FPZ, microcracks form, reactivate and coalesce with each other, which can lead to the development of macroscale discontinuities or fracture surfaces (i.e., macrocracks).

Various models of fracture mechanics have been proposed to describe the plastic zone ahead of crack tips. The Irwin model (1960) quantified the plastic zone by simplifying the stress distribution along the fracture plane. Both Barenblatt (1959) and Dugdale (1960) proposed a strip-yield model that considered the distribution of linear cohesion stress. Labuz, Shah and Dowding (1985) modified the strip-yield model by adjusting the mechanism of microdamage in rocks. Von Mises (1980) introduced a distortion-based criterion to quantify the plastic characteristics of metal. The Schmidt model (1980) incorporated the elastic stress

field ahead of crack tips and solved the boundary condition when the maximum principal stress overcomes the strength. Due to the complex nature of the FPZ, the size and shape of this zone commonly depends on the size of the specimen (Wu, Rong, Zheng, Xu & Dong, 2011; Otsuka & Date, 2000) and size of the crack considered. To understand mechanistically microfracture development and reactivation in the FPZ, a probabilistic response of microcrack dynamics across this zone is required. This response counts the changes in probability—to determine the region of influence—in the active microcracking zone as well as incorporating little to no microcracking in adjacent zones.

3.2 Statistical correlation functions

The development and expansion of fractures is a complex process that can be addressed by a statistical approach that considers the randomness of the fracture network as well as the probability of expansion in a definite direction. Three low-order statistical correlation functions were applied to quantify the progressive expansion of the fracture phase and associated damage to rock specimens. The functions can be applied to material classes such as random heterogeneous materials composed of different materials or phases, amorphous multi-body systems with spherically symmetric potentials and materials with directional bonding (Torquato, 1991; 2002a; 2002b).

We assume that the microstructures resulting from freeze–thaw cycles were static (or approximately static) during times when the rock specimens were maintained at ambient laboratory temperature during pauses in the freeze–thaw cycling for repeated scanning. Therefore, any realisation ω that describes the microstructures of heterogeneous rock materials must be independent of time. A realisation ω of the two-phase random media (i.e., fracture phase and material phase) is based on the probability of occurrence of events described in that realisation and occupies a subset ν in the 3-D Euclidean space, $\nu \in \mathbb{R}$. The disjoint subset ν constitutes the volume fraction of the fracture phase $\nu_{f(}\omega)$ and material phase

$\nu_m(\omega)$. In practice, the indicator function $(x; \omega)$ creates a Boolean array by repeatedly checking a given condition or realisation ω for the fracture phase $x \in (\omega)$ and is defined as

$$\mathbb{I}^f(x;\omega) = \begin{cases} 1, \ if \ x \in \nu_f(\omega), \\ 0, \ otherwise, \end{cases} \quad (1)$$

In each operation, *r* is the distance between the two points considered and *D* is the diameter of the specimen (20 mm). Therefore, the ratio r/D represents the dimension of fracturing activity relative to the diameter of the specimen.

3.2.1 Two-point probability function

For the fracture phase *f*, the two-point probability function S_f is defined as the expectation of the product:

$$(x1; \omega).(x2; \omega) \quad (2)$$

which indicates the probability that the two points *x1* and *x2* belong to the fracture phase. Brown (1955) introduced the n-point probability function to determine the effective directional transport properties in random heterogeneous material. The two-point probability function is a one type of n-point probability function. The function $S_f(r)$ measures how the end points of a vector *r* correlate with each other in the fracture phase. $S_f(r)$ was calculated by randomly projecting line segments of length r (0< r <D) within the defined 3-D space and oriented along a specific direction (Torquato, 1991). A condition that the two end points of the projected line segments belongs to the same fracture phase was checked repeatedly to estimate $S_f(r)$. The boundary conditions for the two-point correlation function are as follows:

$$\lim_{r\to 0} S_{ff}(r,\theta,\phi) = \nu_f \quad (3)$$

$$\lim_{r\to \infty} S_{ff}(r,\theta,\phi) = [\nu_f]^2 \quad (4)$$

where ν_f is the volume fraction of the fracture phase. Eq. (3) indicates that when the separation between the two points approaches zero, the probability of having both the end points in the same phase converges to the volume fraction of the fracture phase. As *r*

increases to infinity (D), the probability of having two end points in the same fracture phase is reduced (Eq. 4). No additional information in between the two bounding points was considered in this function.

In summary, the two-point probability function measures the directional development of the fracture phase irrespective of its continuity. Reiteration of the function after several freeze–thaw cycles captures the progressive development of the fracture phase along predefined directions.

3.2.2 Two-point cluster function

The two-point cluster function (Torquato, 2002b; Torquato, Beasley & Chiew, 1988) (x1,2) calculates the probability of finding any two points x1 and x2 in the same cluster (i.e., adjacent region) of the fracture phase. C_f (x1,2) is useful in determining the connectivity of both the phase distribution and phase cluster, even if the phase connectivity is interrupted by another phase along a specific direction. The boundary conditions for the two-point cluster function are:

$$\lim_{r\to 0} C_f(r,\theta,\phi) = \nu_f \qquad (5)$$

$$\lim_{r\to \infty} C_f(r,\theta,\phi) = 0 \qquad (6)$$

where ν_f is the volume fraction of the connecting fracture phases. Unlike other probability functions, , the probability of finding the two points in the same phase or cluster reaches ν_f (Eq. 5) when the distance between the arbitrarily chosen two points approaches zero. Eq. (6) explains that when the separation between the two points is close to infinity then the chances of getting them in the same phase or cluster approaches zero.

The present study adopted Lee and Torquato's (1989) method to calculate the two-point cluster function. Two points were randomly chosen within the material and it was checked whether these two points belonged to the same phase and cluster. The distance r between the two points was estimated and the process repeated. Further details of the input,

processing and output for both the two-point cluster function and the two-point probability function are given in Maji (2018).

3.2.3 Lineal-path function

The lineal-path function $L_f(r)$ calculates the probability that a line segment of length r lies completely in the fracture phase when randomly placed into the volume space within the material (Torquato, 2002b). Unlike the two-point probability function, the lineal-path function retains phase information at each point on the projected line under consideration and measures the level of continuous connectivity of the fracture phase in a specific direction. The limits for the function are:

$$\lim_{r\to 0} L_f(r,\theta,\phi) = v_f \qquad (7)$$

$$\lim_{r\to \infty} L_f(r,\theta,\phi) = 0 \qquad (8)$$

where v_f is the volume fraction of fracture phase. Eq. (7) indicates that when the length of the test line approaches zero, the probability of finding the same phase at the other end of the moving line converges to the volume fraction of the fracture phase. Conversely, as the length of the test line increases to infinity (Eq. 8), the probability of finding connected fracture phase approaches zero.

The method introduced by Coker and Torquato (1995) to estimate the lineal-path function is modified in the present study, as summarised in a flow chart (Fig. 1). A random point was chosen within the fracture phase in the material, and the phase information in a specific direction was measured by increasing the length of the test line by one unit (i.e., equivalent to the length of one voxel). The process was repeated until the test line encountered a different phase (i.e., the material phase). The process was completed for n = 5000 arbitrarily chosen random points to assess the probabilistic occurrences of continuous line length. This function is more useful than the others as it retains information about the continuous connectivity of the fracture phase. Therefore, the function was applied to 49 varying 3-D

directions (different combinations of azimuth, θ, and zenith angle, ϕ) to quantify the continuity of the developing fracture phase.

4. Results

4.1 Fracture phase

The fracture phase developed progressively during freeze–thaw cycling, as shown by the time series of 3-D visualisations (Fig. 2), 2-D slices (Fig. 3a–f) and photographs of the specimens before (Fig. 3g) and after the experiment (Fig. 3h–i). In chalk, numerous voids too small to see by naked eye but evident from the μ-CT visualisation (green areas in Fig. 2a) existed within the intact specimen prior to freezing. The voids represent the larger (>35 μm) pores naturally present in the intact chalk and detectable by μ-CT scanning. During the first several freeze–thaw cycles, the number and size of voids increased progressively (Fig. 2b–d), representing the initiation and growth of microfractures. Microfracture growth and coalescence, however, did not occur uniformly through the specimen but were concentrated in areas marked by prominent regions of green in Fig. 2e–f, representing macrofractures.

Macrofractures developed in the chalk between cycles 10 and 20 in several regions of microfracture coalescence. Nascent macrofractures had initiated by cycle 15 (Fig. 2e), becoming well developed by cycle 20 (Fig. 2f). Such fractures were vertical and concentric in the upper part of the specimen (Fig. 4b–c), producing more damage there than in the middle and lower parts. A fracture visible near the bottom of Fig. 3c—which depicts a horizontal slice through the upper part of the specimen—was partially developed in cycle 10 along the grain boundary of a fossil fragment that was released by cycle 20. A steeply inclined macrofracture formed during cycles 15 and 20 in the middle of the chalk specimen (Fig. 2e–f), and a weak concentric macrofracture pattern was observed, after cycle 20, near the base.

The sandstone showed fewer new fractures and slower fracture growth than the chalk (Fig. 2g–i). By cycle 20 one macrofracture of moderate size (~10 mm long) and horizontally oriented was apparent in the lower third of the specimen (yellow area in Fig. 2i), and a few smaller ones near the sides. Material that spalled by cycle 20 (Fig. 3f) was induced by a pre-existing void shown in cycles 0 and 10 (Fig. 3d–e). The shape of the fracture observed after 20 cycles followed the outline of the high-entropy material (white granular mass) seen after 0 and 10 cycles that formed a cone around the tabular void. A concentric macrofracture also formed in the lower right part of sandstone between cycles 10 and 20 (Fig. 3f).

4.2 Transverse strain

Transverse strain in the chalk involved mostly dilation and was greatest during the final five freeze–thaw cycles (Fig. 4). During the first 10 cycles, 22 of 25 marker pairs indicated dilation in the cross section through the middle of the chalk cylinder (Fig. 4a), though 3 pairs indicated some contraction in the middle of the core, as shown in the inset in Fig. 4a. Before cycle 10, the range in strain was less than 0.04%. Strain measured by the last 5 cycles increased substantially, ranging between 0.05–0.07% in cycle 15 and 0.14–1.2% in cycle 20. The markers located in the upper part of chalk experienced relatively higher strain compared to markers situated near the middle and lower part of the specimen (Fig. 4b). The sandstone core, on the other hand, experienced 0.01–0.02% strain and no such variations along the axial dimension were observed.

4.3 Statistical correlation functions

4.3.1 Two-point probability function

The two-point probability function compares the distribution of the fracture phase along horizontal (X, Y) and vertical (Z) directions in the rock specimens as the number of

freeze–thaw cycles increased (Fig. 5). When the r/D ratio is low, the probability of obtaining the fracture phase is high, whereas when the ratio is high (i.e., the extent of microfracturing dissipates beyond the dimension of the specimen) the probability approaches zero.

For chalk, along the three principle directions (X, Y, Z), for < 0.05 r/D, the higher probability values for all cycles indicate the extent of inherent defects in that direction. Values of $S_f(r)$ > 0.4 for each direction describe the inheritance of material microflaws, whereas values < 0.4 and > 0 illustrate the accumulation of microfractures during freezing and thawing (Fig. 5a–c). Distinct peaks and troughs in the values of $S_f(r)$ can be identified, particularly in the X- and Z-directions in cycle 20. The limit of intense microcracking activity after 20 cycles varies along the X-, Y- and Z-directions for $S_f(r)$ = 0.05, with r/D values of 0.25, 0.09 and 0.38, respectively. Thus, the function indicates that vertical accumulation of microfractures exceeded horizontal accumulation. Substantial changes in $S_f(r)$ occurred between the first 15 cycles and cycle 20. The maximum changes occurred along the Z-direction, where the value of $S_f(r)$ remains above zero for a distance up to r/D = 0.4, whereas for the X- and Y-directions, the r/D ratio is 0.3 and 0.2, respectively. The high $S_f(r)$ values along the Z-direction explain the vertical fractures observed in the chalk.

For sandstone, the two-point probability function shows that the fracture phase developed more along the X- and Y-directions than along the Z-direction (Fig. 5d–f). This is consistent with the horizontal lamination in the sandstone. Higher $S_f(r)$ values and a high r/D ratio (0.25) are found in the Y-direction relative to the X-direction during all the cycles. The anomaly in the Y-direction is consistent with the scanned images, which reveal major inherited voids and flaws oriented along the Y-direction (Fig. 3d–f).

4.3.2 Two-point cluster function

The two-point cluster function documents small changes in probability (< 1%) compared to the other functions in order to describe the network or connectivity of the fracture phase.

The probability of finding two random points in this phase irrespective of any directional constraint is < 10% in both the chalk and the sandstone (Fig. 6). As the number of freeze–thaw cycles increases, the changes in $C_f(r)$ are relatively high when the r/D ratio is < 0.1 (0.1 r/D = 2 mm), but decrease as the ratio increases. Overall, the function shows that the connectivity within the fracture phase in chalk increased progressively as the number of freeze–thaw cycles increased, whereas the connectivity in sandstone increased from cycles 0 to 10 but decreased by cycle 20.

4.3.3 Lineal-path function

Before we report the results from the lineal-path function, we define and illustrate the parameters that describe the different segments of the function based on the similarities and differences observed in 49 directions (Fig. 7a). The values of the function for different cycles followed a similar trajectory at the beginning, when the distance $r \rightarrow 0$. The maximum dimension (r/D) of length common to all cycles defines the *initial consistent limit* (i.e., the extent of inherent flaws). Conversely, when the distance $r \rightarrow D$, the trajectory of the curves for different cycles again merges with each other, which is described by the *end limit for the active crack length*. The region between these limits—where the trajectory of the curves for different cycles changed progressively—is termed the *length of active crack region*. Within this region the activity, expressed in terms of changes in $L_f(r)$, is higher than in the regions on either side. The r/D ratio indicates the continuity (i.e., length) of the fracture phase. The length at cycle 0 is termed the *minimum crack length*, and the length after cycle 20 the *maximum crack length*. To determine the progressive development of the continuous fracture phase along various linear directions, lineal-path functions were compared for different cycles along various orientations of θ and ϕ.

Fig. 7b exemplifies the lineal-path function for chalk (θ = 90°, ϕ = 60°) and Fig. 7c for sandstone (θ = 30°, ϕ = 120°). In chalk, the trajectory for the initial 10 cycles followed a similar

path, but by cycles 15 and 20 small increases in $L_f(r)$ in the length of the active region were apparent (Fig. 7b). In sandstone, the changes in $L_f(r)$ between the initial and final cycle were minimal, but the small increment in the continuous fracture phase is noted (Fig. 7c). In both rock types, the continuous line length of the fracture phase—based on the probabilistic occurrences of the 5000 random points—increased progressively as the number of cycles increased.

Summary data on the increments in $L_f(r)$ and line length for different combinations of θ and ϕ during the 20 freeze–thaw cycles are presented in boxplots for the chalk and sandstone specimens (Fig. 8). The maximum changes in $L_f(r)$ of 9% were noted in chalk (median = 6%), when $\phi = 0°$ (Fig. 8a), which indicates growth in the horizontal direction, whereas the sandstone maintained an average $L_f(r)$ value of 2% along all the different directions (Fig. 8b). The maximum increment in the length of continuous fracture phase in chalk was observed in the vertical direction ($\phi = 90°$; median = 1.58 mm) and the minimum increment in the horizontal orientation ($\phi = 0°$; 0.94 mm) (Fig. 8c), indicating maximum continuity for vertical fractures. The overall average increment in the length of continuous fracture phase in chalk (1.38 mm) was an order of magnitude greater than that in sandstone (0.25 mm) (Fig. 8c–d). The full dataset, with individual boxplots for each of the 49 directions, is presented in Maji (2018).

5. Discussion

5.1 Rock fracture

The application of repeated μ-CT scanning to image progressive rock fracture during intervals freeze–thaw cycling demonstrates the potential of this method in laboratory studies of slow frost weathering process. Micro-CT successfully imaged in 3-D the growth and coalescence of microfractures larger than 35 μm into macrofractures (Fig. 2) that were verified by observation of the rock specimen at the end of the experiment (Fig. 3i). It also

revealed that some pre-existing structures such as fossil fragments (Fig. 3c) and high-entropy material (Fig. 3e) acted as weak planes if encountered by propagating microfractures, favouring macrofracture development and sometimes spalling (Figs. 3f and 3j).

The cause of rock fracture initiation by freeze–thaw cycling in the experiment is unclear. Ice segregation seems unlikely, because ice lenses formed during downward freezing from a horizontal surface tend to be horizontal, as shown in a previous experiment using 20 mm cubes of the same chalk type (Murton et al., 2001), unlike the concentric vertical fractures observed in the present one. However, we cannot rule out the possibility that the geometry of the core cylinders in the microscale experiment may have induced near-surface vertical fracturing, if some inward freezing occurred, causing water to migrate outward toward the sides of the cylinder and supply vertical ice lenses. Alternative possibilities for the development of the observed vertical fractures in the chalk include desiccation (freeze–drying; Mackay, 1974), thermal contraction (Murton, Ozouf & Peterson, 2016), some combination of the two, or thermal fatigue (Jia, Xiang & Krautblatter, 2015; Hall, 1999). Further experiments using rock specimens at varying moisture contents are needed to elucidate the cause of fracturing.

5.2 Strain

Transverse strain recorded during freeze–thaw cycling of the chalk specimen (Fig. 4) indicates dilation perpendicular to the axial dimension as vertical fractures formed. Strain measured near the top of the specimen exceeded that in the middle and lower parts, suggesting that the fractures initiated near the top and propagated downward. Until cycle 15, the transverse strain measured at various depths of the chalk was limited to 0.07%, whereas by cycle 20 it had increased to between 0.14 and 1.2%. The 1–2 orders-of-magnitude increase in strain between cycles 15 and 20 suggests this was associated with the initiation, reactivation and extension of macrofractures, consistent with 3-D visualisations of the

evolving macrofracture network in cycles 15 and 20 (Fig. 2e–f). Interestingly, Azmatch, Arenson, and Sego (2008) noted similar horizontal strain in Devon silt attributed to formation of vertical tension fractures. The higher tensile strength of chalk compared to silt is thought to delay the onset of fracturing in the present experiment.

5.3 Statistical correlation functions

The two-point probability function—which measures the growth of the fracture phase along the X-, Y- and Z-directions even if the fracture phase is not continuous—showed that fracturing developed along all three orthogonal directions as the number of freeze–thaw cycles increased in both rock types. Particularly in chalk, the growth in the vertical (Z) direction exceeded that in the horizontal (X and Y) direction, which is confirmed both by the concentric vertical fractures visualised by μ-CT scanning (Fig. 2e–f) and observed by eye (Fig. 3i). The large peaks and troughs in values of $S_f(r)$ may represent the highly localised development of fractures in a number of regions along that direction. Sandstone, on the other hand, recorded relatively more growth of the fracture phase along the horizontal plane than the vertical direction, which suggests that fractures preferentially developed along the horizontal lamination within the rock. Applying the two-point probability function alone, however, is not sufficient to reconstruct the internal morphology of anisotropic material, and incorporating the lineal-path function improves the accuracy (Yeong & Torquato, 1998).

The lineal-path function and the parameters that define segments of the curve provide a method to quantify non-reversible damage in anisotropic rock along various directions during freeze–thaw cycling. This new classification is based on superimposing results from repeated scans of the same specimens. The parameters serve to distinguish directional continuous growth above the average threshold conditioned by inherent flaws in rock. As described in section 4.3.3, the maximum increment in the length of continuous fracture phase in the chalk was observed in the vertical direction ($\phi = 90°$) followed by the horizontal orientation ($\phi = 0°$)

(Fig. 8c). The increase in continuous length along the vertical direction suggests the vertical fractures developed maximum continuity. The formation of concentric vertical fractures accompanied by dilation (noted in pixel-based strain measurement; Fig. 4a) increased the probability of linear growth in the horizontal direction relative to other directions (radial expansion near the specimen boundary). Such increased probability of horizontal growth may indicate the influence of imposing a vertical thermal gradient. It is suggested that microfractures propagating horizontally had not yet coalesced to form visible macrofractures.

For sandstone, the average change in $L_f(r)$ is 2.17% compared to 6.49% for chalk, which indicates that the sandstone was less damaged than the chalk (Fig. 8a–b) after 20 freeze–thaw cycles. This result is also consistent with the compressive and tensile strength of sandstone (1–2 orders of magnitude higher than that of the chalk) and with the linear development of the fracture phase (three times lower than that of the chalk). The average linear growth after 20 cycles for chalk and sandstone was 1.38 and 0.25 mm, respectively (Fig. 8c–d). Increases in $L_f(r)$ and increments in continuous line length of the fracture phase weaken material as the number of cycles increases. A similar phenomenon was described by Jia et. al., (2015) as a fatigue effect as the number of freeze–thaw cycles increases.

In terms of the two-point cluster function—which assesses the strength of the network within the same fracture phase irrespective of morphology or directional constraints—the change in the $C_f(r)$ is noticeably low (<0.2) compared to the changes in $S_f(r)$ and $L_f(r)$. Development of the fracture phase around the dimension of inherent flaws was noticeably high ($r/D < 0.05$), which suggests the cluster of the fracture phase around inherent flaws may be due to the effect of stress concentration. The higher $C_f(r)$ value of sandstone than chalk before freezing (cycle 0) indicates that the inherent connectivity within sandstone was greater than that within chalk. The function increased progressively in chalk, whereas in sandstone it decreased during the final freeze-thaw cycle.

5.4 Classification of microcracking zones

As the macroscopic property of interest of a material is a function of appropriate local fields weighted with definite correlation functions (Torquato, 2002b), a new approach in the present study was undertaken using the lineal-path function to define and quantify different zones of microfracturing during freeze–thaw cycling of anisotropic rock. Three zones are distinguished based on the probabilistic occurrence and extent of the fracture phase during freeze–thaw (Fig. 9):

(1) The *zone of inherent flaws* in both the chalk and sandstone was nearly the same and is thought to reflect the size of some of the pores between mineral grains. The dimension of the inherent flaws in the medium to fine-grained sandstone (Radley & Allen, 2012) is 0.13 mm, which lies within fine-sand category of particle size. In chalk, the dimensions of inherent flaws is 0.12 mm (i.e., equivalent to very fine sand). As the chalk contains abundant detrital quartz and fossil fragments, the zone of inherent flaws reached the very fine sand category rather than showing silt- or clay-size flaws.

(2) The *zone of active microcracking* was more extensive in chalk than sandstone (1.01 and 0.71 mm, respectively), which signifies greater damage in chalk. Comparing the extent of this zone along various directions can quantify damage. The zone active of microcracking ahead of the zone of inherent flaws can be considered as the plastic zone (FPZ) ahead of crack tips, following the theoretical models of nonlinear fracture mechanics (Irwin, 1960; von Mises, 1913). The progressive growth of this zone during the course of 20 freeze–thaw cycles may be consistent with the growing FPZ ahead of crack tips.

(3) The *zone of weak influence during microcracking* showed values of $L_f(r)$ of nearly zero, though the end limit of this zone was more extensive (2.16 and 1.81 mm for chalk and sandstone, respectively) than in the other zones. Overall, the very low probabilities in this zone denote limited microcracking activity in it.

The different methods of analysis that relate the particle size of the rock types—which indirectly relates to porosity—with the probability function confirms that the model replicates the inherent flaw zone. This analysis therefore justifies the spatial extent of the FPZ around inherent flaws in a probabilistic way by incorporating multiple flaws (n = 5000) rather than tracking the dynamics of a single hole or flaw. Damage within material can be considered as the changes in the behaviour of inherent flaws and how they expand under loading—cyclic loading, with external physical stimuli such as freeze–thaw cycling in the present study. The probabilistic method replicated the growth of multiple inherent microflaws on a probability scale and classified different microcracking zones based on changes in probability during microcrack extension.

6. Conclusions

The present research aims to understand the early stages of rock fracture in limestone (chalk) and sandstone by applying advanced micro-CT imaging and statistical methods to a frost-weathering experiment. The specimens were scanned and visualised at various intervals during 20 freeze–thaw cycles and a novel classification method is introduced to quantify rock fracture. The evaluation of the experimental analysis finds the following conclusions.

(1) The application of repeated μ-CT scanning is demonstrated to visualise the early stages of microfracturing during frost weathering of intact rock samples. The non-destructive method allowed 3-D visualisation of the growth and coalescence of microfractures larger than 35 μm and their transition into macrofractures.

(2) Greater and quicker frost damage occurred in the chalk specimen than in the sandstone, as revealed by μ-CT visualisations, estimates of transverse strain, observations of macrofractures at the end of the experiment and probabilistic modelling of microcracking.

(3) Two different analyses of repeated μ-CT images suggest that the degree of damage in chalk crossed a threshold beyond which the damage accelerated and extended. Transverse strain estimates revealed substantial dilation of the chalk occurred after cycle 15. The two-point probability and lineal-path functions also indicated substantial changes in the probability index after cycle 15. Both methods suggest that fatigue effects (i.e., gradual and limited rock damage) characterise the early cycles and if the material passes a threshold, the damage may proceed quickly and become more prominent.

(4) The modified lineal-path function is particularly useful in quantifying rock fracture by freeze–thaw because it measures the connectivity of the continuous fracture phase in a specific direction. The continuity of the fracture phase can be assessed in multiple directions and during multiple freeze–thaw cycles, allowing distinction of three zones of microcracking activity, based on nonlinear fracture mechanics theory.

(5) The *zone of inherent flaws* reflects the size of some of the pores between mineral grains and follows the sedimentary particle-size scale. The *zone of active microcracking* is thought to represent the evolution of the plastic zone (FPZ) ahead of the crack tip and is quantified based on the number of random situations (samples) rather than replicating the mechanics for a single circular or elliptical hole. The *zone of weak influence during microcracking* experiences limited fracture.

In terms of limitations of this study, some interruptions occurred during scanning after freeze–thaw cycles 6 and 8 as the chalk specimen was not completely dried and so the scans were discarded in the present study. Moisture within the rock during scanning significantly shifts the grey scale range and induces error. The frost weathering experiment successfully developed fractures in chalk. However, fracturing of the harder Ardingly Sandstone would require more freeze–thaw cycles. Future research should ensure greater repeatability of the

experiments and test a wider range of rock types. A new approach is introduced using the lineal path function to classify different zones of microcracking based on their probabilistic occurrence. It is identified that the damage zone ahead of the inherent flaws resembles the plastic zone ahead of the crack tip. More analysis is required to correlate the extent of these two zones.

Appendices

Appendix A.

Table A.1.

Acquisition parameters for μ-CT scanning

Target metal	Tungsten
Filter	1 mm thick copper
Voltage	186 kV
Current	250 μA
Exposure time	1000 ms
Gain	12 dB
Digital gain	1X
Number of projections	1571
Number of images for shading correction	3
Frames to average	4

Table A.2.

Workflow of the μ-CT analysis

Task	**Step**	**Process**
Acquisition	Sample preparation	Prepare 30 mm long and 20 mm diameter core plugs using drilling and grinding techniques
	Set up live imaging	Set up and lock the position of the rotating stage to ensure the object is under the detector for all the positions in a 360° rotation and repeated scan
	Set up μ-CT scan	Set the acquisition parameters in Inspect X software
Reconstruction	Transfer data to reconstruction PC	Save and transfer data from acquisition PC to reconstruction PC
	Reconstruction	Reconstruct 2-D projections into 3-D volume using CT-Pro software

Rendering	Convert to RAW	Convert image to RAW format for easy handling using Image J software
	Drishti import	Import RAW images into Drishti Import for further operation in Drishti
	Visualisation	Visualise the 3-D volume of the specimen in Drishti using transfer function
Analysis	Data analysis	Convert image information into matrix form for analysis in Matlab

Acknowledgements

This research is part of the senior author's doctoral research at the University of Sussex. The research was funded by a Chancellor's international research scholarship and a Global Studies studentship in the Department of Geography. Tim Cane provided valuable help and guidance with experimental design, sample preparation and use of the climate cabinets in the Permafrost Laboratory. Dr. Simon Carr, Lucy Diggens and Michele Day at the Centre for Micromorphology, Queen Mary University, London, are thanked for providing access to micro-computing tomography and guidance about image processing and analysis. Comments from Drs P. Cleall and J. Barlow on an earlier version of the manuscript and from Dr. L. Arenson and an anonymous referee of the present manuscript are appreciated.

References

Azmatch, T. F., Arenson, L. U, & Sego, D. C. (2008, 29 June–3 July). Measuring ice lens growth and development of soil strains during frost penetration using particle image velocimetry (GeoPIV). In Kane, D L., & Hinkel, K. M. (Eds.), *Proceedings of the 9th International Permafrost Conference, University of Alaska Fairbanks.* (Vol. 1, pp. 89–93), Fairbanks: Institute of Northern Engineering, University of Alaska Fairbanks.

Ballantyne, C. K. (2018). *Periglacial Geomorphology*. Chichester: Wiley.

Barenblatt, G. I. (1959). The formation of equilibrium cracks during brittle fracture. General ideas and hypotheses. Axially-symmetric cracks. *Journal of Applied Mathematics and Mechanics, 23(3)*, pp. 622–636. https://doi.org/10.1016/0021-8928(59)90157-1

Brown, W. F. (1955). Solid mixture permittivities. *The Journal of Chemical Physics, 23(8)*, pp. 1514–1517. https://doi.org/10.1063/1.1742339

Bultreys, T., Boone, M.N., Boone, M.A., De Schryver, T., Masschaele, B., Van Hoorebeke, L., & Cnudde, V. (2015). Fast laboratory-based micro-computed tomography for pore-scale research: Illustrative experiments and perspectives on the future. *Advances in Water Resources, 8*, pp. 55–1. doi:10.1016/j.advwatres.2015.05.012

Cnudde, V., & Boone M. N. (2013). High-resolution X-ray computed tomography in geosciences: A review. *Earth-Science Reviews,* (123), pp. 1–17. https://doi.org/10.1016/j.earscirev.2013.04.003

Coker, D. A., & Torquato, S. (1995). Extraction of morphological quantities from a digitized medium. *Journal of Applied Physics,* 77(12), pp. 6087–6099. https://doi.org/10.1063/1.359134

Dugdale, D. (1960). Yielding of steel sheets containing slits. *Journal of the Mechanics and Physics of Solids,* 8(2), pp. 100–104. https://doi.org/10.1016/0022-5096(60)90013-2

Griffiths, A. A. (1921). The phenomena of rupture and flowin solids. *Philosophical Transactions of the Royal Society A, London,* (221), pp. 163–198. https://doi.org/10.1098/rsta.1921.0006

Griffith, A. A. (1924). Theory of rupture. In Biereno, C. B., Burgers, J. M., & Waltman, J. Jr. (Eds.), *Proceedings of the 1st International Congress for Applied Mechanics, Delft, (*pp. 55–63), Delft.

Hall, K. (1999). The role of thermal stress fatigue in the breakdown of rock in cold regions. *Geomorphology, 31*, 47–63. https://doi.org/10.1016/S0169-555X(99)00072-0

Hoagland, R. G., Hahn, G. T., & Rosenfield, A. R. (1973). Influence of microstructure on fracture propagation in rock. *Rock Mechanics, 5(2)*, pp. 77–106. https://link.springer.com/article/10.1007/BF01240160

Im, S., Kim, Y.-R., & Ban, H. (2013). Rate- and temperature-dependent fracture characteristics of asphaltic paving mixtures. *Journal of Testing and Evaluation, 41(2)*, pp. 257–268. https://doi.org/10.1520/JTE20120174

Irwin, G. R. (1960). Plastic zone near a crack and fracture toughness. *Proceedings of the 7th Sagamore Ordnance Materials Research Conference*. *Vol. 4*. New York: Syracuse University, pp. 63–78.

Jia, H., Xiang, W., & Krautblatter, M. (2015). Quantifying rock fatigue and decreasing compressive and tensile strength after repeated freeze-thaw cycles. *Permafrost and Periglacial processes, 26(4)*, pp. 368–377. https://doi.org/10.1002/ppp.1857

Labuz, J., Shah, S., & Dowding, C. (1985). Experimental analysis of crack propagation in granite. *International Journal of Rock Mechanics and Mininig Sciences & Geomechanics Abstracts, 22(2)*, pp. 85–98. https://doi.org/10.1016/0148-9062(85)92330-7

Lee, S. B., & Torquato, S. (1989). Measure of clustering in continuum percolation: computer-simulation of the two-point cluster function. *The Journal of Chemical Physics, 91(2)*, pp. 1173–1178. https://doi.org/10.1063/1.457190

Mackay, J. R. (1974). Reticulate ice veins in permafrost, northern Canada. *Canadian Geotechnical Journal.*, *11*, pp. 230–237. https://doi.org/10.1139/t74-019

Maji, V. (2018). *An experimental investigation of micro- and macrocracking mechanisms in rocks by freeze–thaw cycling*. [PhD thesis]. Brighton: University of Sussex. http://sro.sussex.ac.uk/79661/

Mises, R. (1913). Mechanik der festen Körper im plastisch-deformablen Zustand (Mechanics of solid bodies in plastically deformable state). *Nachrichten von der Gesellschaft der Wissenschaften zu Göttingen, Mathematisch-Physikalische Klasse,* pp. 582–592. http://www.digizeitschriften.de/dms/resolveppn/?PID=GDZPPN002503697

Murton, J. B., Coutard, J. P., Lautridou, J.P., Ozouf, J.C, Robinson, D.A., Williams, R. B. G., Guillemet, G., & Simmons, P. (2000). Experimental design for a pilot study on bedrock weathering near the permafrost table. *Earth Surface Processes and Landforms, 25(12)*, pp. 1281–1294. https://doi.org/10.1002/1096-9837(200011)25:12<1281::AID-ESP137>3.0.CO;2-U

Murton, J.B., Coutard, J.-P., Ozouf, J.-C., Lautridou, J.-P, Robinson, D. A., & Williams, R. B. G. (2001). Physical modelling of bedrock brecciation by ice segregation in permafrost. *Permafrost and Periglacial processes, 12*, pp. 255–266. https://doi.org/10.1002/ppp.390

Murton, J. B., Peterson, R., & Ozouf, J. C. (2006). Bedrock fracture by ice segregation in cold regions. *Science, (314)*, pp. 1127–1129. https://doi.org/10.1126/science.1132127

Murton, J. B., Ozouf, J.-C., & Peterson, R. (2016). Heave, settlement and fracture of chalk during temperature cycling above and below 0°C. *Geomorphology, 270*, pp. 71–87. https://doi.org/10.1016/j.geomorph.2016.07.016

Murton, J. B. (2018, 17–*18* September). Frost weathering of chalk. In Lawrence, J. A., Preene, M., Lawrence, U. L., & Buckley, R. (Eds.), *Engineering in Chalk: Proceedings of the Chalk 2018 Conference, Imperial College, London* (pp. 497–502), London: ICE Publishing.

Otsuka, K., & Date, H. (2000). Fracture process zone in concrete tension specimen. *Engineering Fracture Mechanics, 65(2–3)*, pp. 111–131. https://doi.org/10.1016/S0013-7944(99)00111-3

Radley, J. D., & Allen, P. (2012). The Wealden (non-marine Lower Cretaceous) of the Weald Sub-basin, southern England. *Proceedings of the Geologists' Association, 123(2)*, pp. 245–318. https://doi.org/10.1016/j.pgeola.2012.01.003

Schmidt, R. A. (1980, 27–30 May). A microcrack model and its significance to hydraulic fracturing and fracture toughness testing. In *The 21st U.S. Symposium on Rock Mechanics* (pp. 581–590.ARMA–80–0581), Rolla: The University of Missouri.

Shiklomanov, N.I., Streletskiy, D. A., Grebenets, V. I., & Suter, L. (2017). Conquering the permafrost: urban infrastructure development in Norilsk, Russia. *Polar Geography, 40(4)*, pp. 273–290. https://doi.org/10.1080/1088937X.2017.1329237

Torquato, S., Beasley, J. D., & Chiew, Y. C. (1988). Two-point cluster function for continuum percolation. *The Journal of Chemical Physics, 88(10)*, pp. 6540–6547. https://doi.org/10.1063/1.454440

Torquato, S. (1991). Random heterogeneous media: microstructure and improved bounds on effective properties. *Applied Mechanics Reviews, 44(2)*, pp. 37–76. doi:10.1115/1.3119494

Torquato, S. (2002a). Statistical description of microstructures. *Annual Review of Materials Research, 32(1)*, pp. 77–111. https://doi.org/10.1146/annurev.matsci.32.110101.155324

Torquato, S. (2002b). *Random Heterogeneous Materials: Microstructure and Macroscopic Properties*. New York:Springer-Verlag.

Vlahou, I. (2012). *Freeze fracturing of elastic porous media*. [PhD thesis]. Cambridge: University ofCambridge.

Vlahou, I., & Worster, M. G. (2015). Freeze fracturing of elastic porous media: a mathematical model. *Proceedings of Royal Society A-Mathematical, Physical and Engineering Sciences, 471(2175).* http://dx.doi.org/10.1098/rspa.2014.0741

Williams, R. B. G., & Robinson, D. A. (1981). Weathering of sandstone by the combined action of frost and salt. *Earth Surface Processes and Landforms, (*6), pp. 1–9. https://doi.org/10.1002/esp.3290060102

Williams, R. B. G., & Robinson, D. A. (2001). Experimental frost weathering of sandstone by various combinations of salts. *Earth Surface Processes and Landforms, (26)*, pp. 811–818. https://doi.org/10.1002/esp.227

Wu, Z., Rong, H., Zheng, J., Xu, F., & Dong, W. (2011). An experimental investigation on the FPZ properties in concrete using digital image correlation technique. *Engineering Fracture Mechanics, 78(17)*, pp. 2978–2990. https://doi.org/10.1016/j.engfracmech.2011.08.016

Yeong, C. L. Y., & Torquato, S. (1998). Reconstructing random media. II. Three-dimensional media from two-dimensional cuts. *Physical Review E, 58 (224)*, pp. 224–233. https://doi.org/10.1103/PhysRevE.58.224

Figure captions

Fig. 1. Flow chart summarising the input, processing and output for the lineal-path function.

Fig. 2. 3-D visualisations of the developing fracture phase (green in a–f; yellow in g–i) in specimens of chalk (a–f) and sandstone (g–i) after different freeze–thaw cycles. Prominent fracture surfaces (macrocracks) had developed by cycle 20 in the chalk (f), with those near the top having a concentric vertical form. The cylindrical outline of the specimens is apparent and oriented relative to three orthogonal axes (X: red, Y: green, Z: blue). The top of the specimens is near the top of each panel.

Fig. 3. 2-D μ-CT image slices orthogonal to the vertical axis of the chalk (a–c) and sandstone (d–f) specimens after 00, 10 and 20 freeze–thaw cycles. In the chalk, a macrocrack (black) near a fossil fragment (white) initiated and developed between cycles 10 and 20 to form a well-developed concentric crack. In the sandstone, some material spalled off around the large void (black) between cycles 10 and 20. Major inherited voids in the sandstone are oriented along the Y-direction. Photographs of the chalk and sandstone specimens before (g) and after (h–j) the freeze–thaw experiment. Vertical cracks are evident in the chalk (h–i). (i) Shows a view of concentric vertical cracks, as seen looking down onto the top of the chalk specimen. (j) Shows a void left by spalled material in sandstone.

Fig. 4. Measurements of transverse strain of the chalk specimen plotted through time (a) and against depth (b), determined from 25 marker pairs, after different freeze–thaw cycles. Inset in (a) shows details during cycles 1–10. Time series depth slices of chalk in (b) illustrate the position of a marker pair.

Fig. 5. Two-point probability functions for chalk (a–c) and sandstone (d–f) along orthogonal directions (X, Y, Z) after different freeze–thaw cycles. ‘r’ is the distance between two points; ‘D’ is the diameter of the rock specimen.

Fig. 6. Two-point cluster functions for chalk (a) and sandstone (b) along orthogonal directions (X, Y, Z) after different freeze–thaw cycles. ‘r’ is the distance between two points; ‘D’ is the diameter of the rock specimen.

Fig. 7. (a) Classification plot of the parameters that describe the different segments of the lineal-path probability functions along a specific 3-D direction for different freeze–thaw cycles. The *initial consistent limit* denotes the small length of inherent flaws within the material which is not affected by the number of cycles. *The active length region* is the zone ahead of inherent flaws (crack tips) where noticeable change in probability—$L_f(r)$—occurred between initial and final cycles. The *end limit of active crack region* is marked by the condition when $L_f(r)$ values of different cycles again merge with each other at near-zero values. The *minimum and maximum crack length* denote the length of the continuous fracture phase before the first cycle and after the final cycle. Lineal-path probability functions for chalk (b) and sandstone (c) in one of 49 predefined 3-D directions. ‘r’ is the distance between two points; ‘D’ is the diameter of the rock specimen. Note different range of y axis in both plots, and the maximum value of r/D on the x axis is not 1 (as in Figs. 5–6) but 0.1.

Fig. 8. Boxplots showing the increment in the probability values of Lf(r) and in the continuous line length (i.e., difference between maximum and minimum crack length) between 00 and 20 freeze–thaw cycles for 49 different (various combinations of θ and φ) 3-D directions for (a & c) chalk and (b & d) sandstone. Each φ (zenith angle) direction on the X-axis is weighted with seven θ (azimuth angle) directions, as shown by the arrows within the ellipses; thus each boxplot summarises changes in 7 directions. Horizontal red lines indicate median values. The

average probabilistic increment in the zone of active crack and the average increment in the continuous line length in chalk and sandstone are 6 & 2% and 1.38 & 0.26 mm, respectively.

Fig. 9. Summary diagram integrating fracture mechanics concepts (a–b) with the microcracking zones identified in this study (c) relative to a sediment particle-size scale (d). (a) Illustrates schematically the development of the fracture process zone (FPZ) of an existing crack under tension. (b) Shows the mechanical changes across the FPZ; cohesive-zone traction (T) reaches a peak value, or cohesive strength (Tmax); ∂c is the cohesive-zone displacement. (c) Shows a graph of the linear-path function for one of the 49 directions simulated in the chalk specimen as a reference for the three newly classified microcracking zones, whose relative lengths (mm) are tabulated. Changes in Lf(r) are maximal in the FPZ, but negligible in the other two zones. The changes in the probability imply the development of existing microcracks in the FPZ. (d) The sediment particle-size scale relates the texture of the chalk and sandstone to the extent of the zone of inherent flaws (i.e., inherited microfabric). Sources: (a) and (b) from ref. (Im, Kim & Ban, 2013), and (d) from https://pubs.usgs.gov/of/2006/1195/htmldocs/nomenclature.htm.

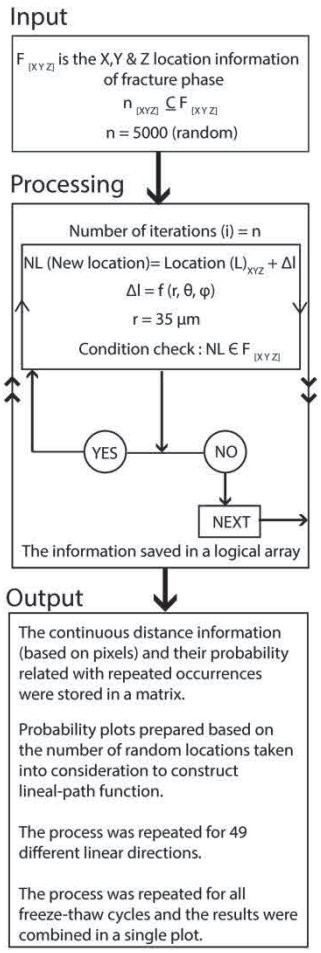

Fig. 1. Flow chart summarising the input, processing and output for the lineal-path function.

209x296mm (300 x 300 DPI)

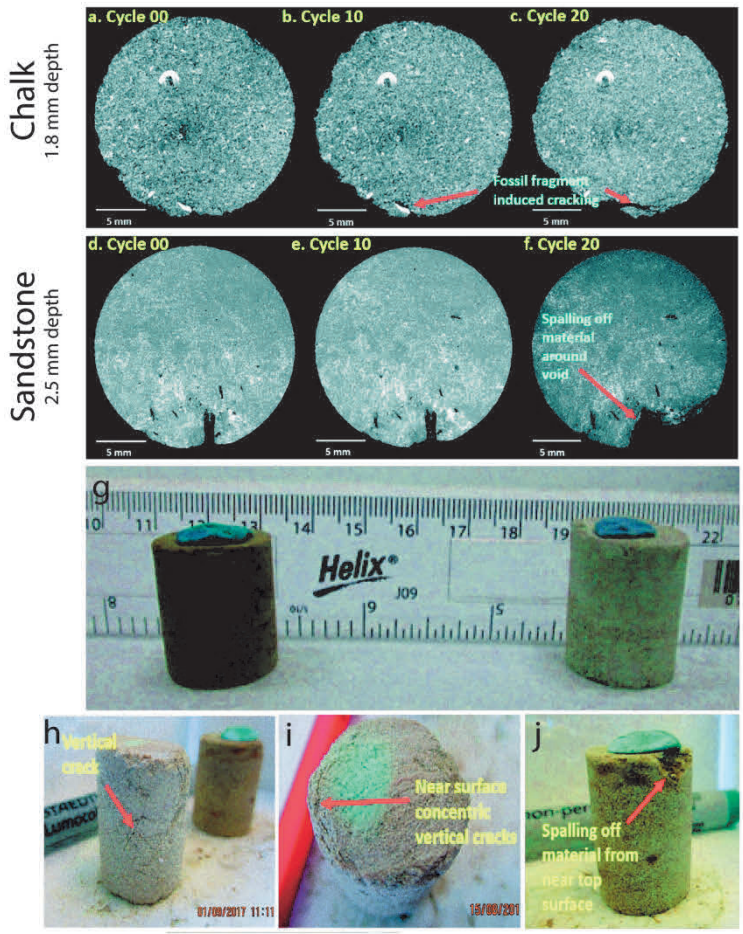

Fig. 3. 2-D μ-CT image slices orthogonal to the vertical axis of the chalk (a–c) and sandstone (d–f) specimens after 00, 10 and 20 freeze–thaw cycles. In the chalk, a macrocrack (black) near a fossil fragment (white) initiated and developed between cycles 10 and 20 to form a well-developed concentric crack. In the sandstone, some material spalled off around the large void (black) between cycles 10 and 20. Major inherited voids in the sandstone are oriented along the Y-direction. Photographs of the chalk and sandstone specimens before (g) and after (h–j) the freeze–thaw experiment. Vertical cracks are evident in the chalk (h–i). (i) Shows a view of concentric vertical cracks, as seen looking down onto the top of the chalk specimen. (j) Shows a void left by spalled material in sandstone.

209x296mm (300 x 300 DPI)

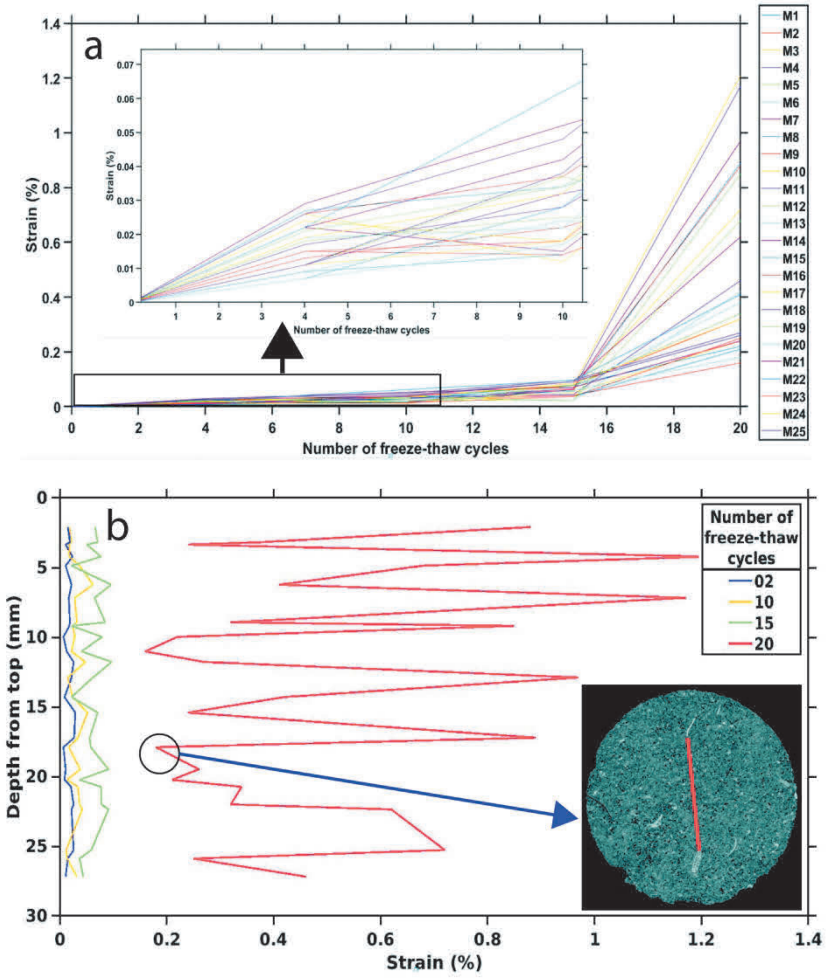

Fig. 4. Measurements of transverse strain of the chalk specimen plotted through time (a) and against depth (b), determined from 25 marker pairs, after different freeze–thaw cycles. Inset in (a) shows details during cycles 1–10. Time series depth slices of chalk in (b) illustrate the position of a marker pair.

209x296mm (300 x 300 DPI)

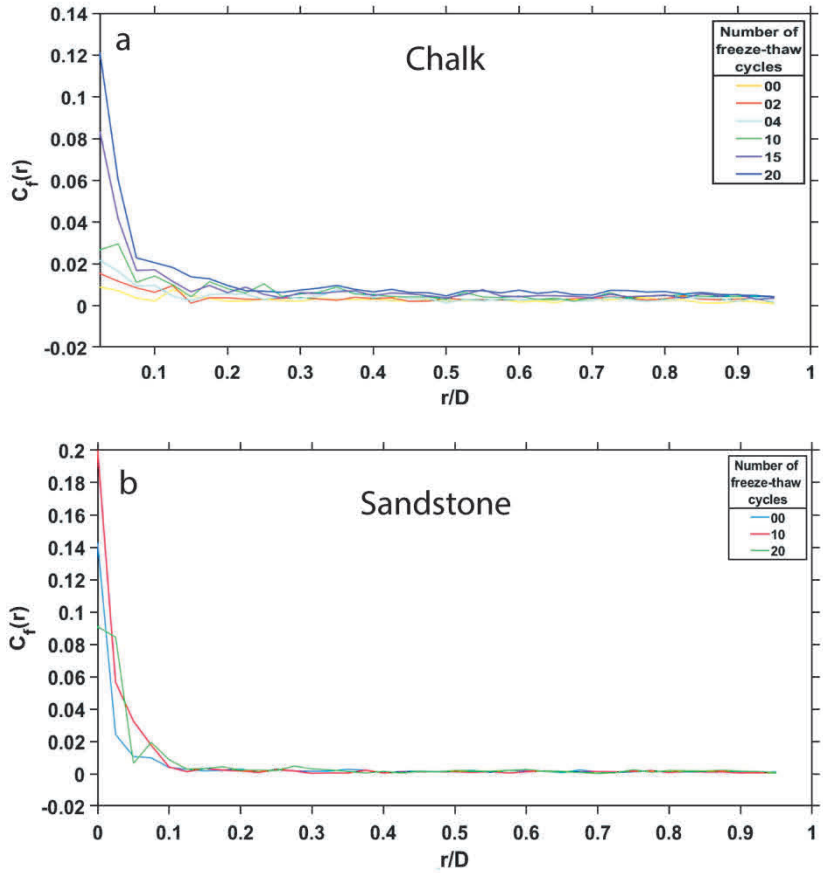

Fig. 6. Two-point cluster functions for chalk (a) and sandstone (b) along orthogonal directions (X, Y, Z) after different freeze–thaw cycles. 'r' is the distance between two points; 'D' is the diameter of the rock specimen.

209x296mm (300 x 300 DPI)

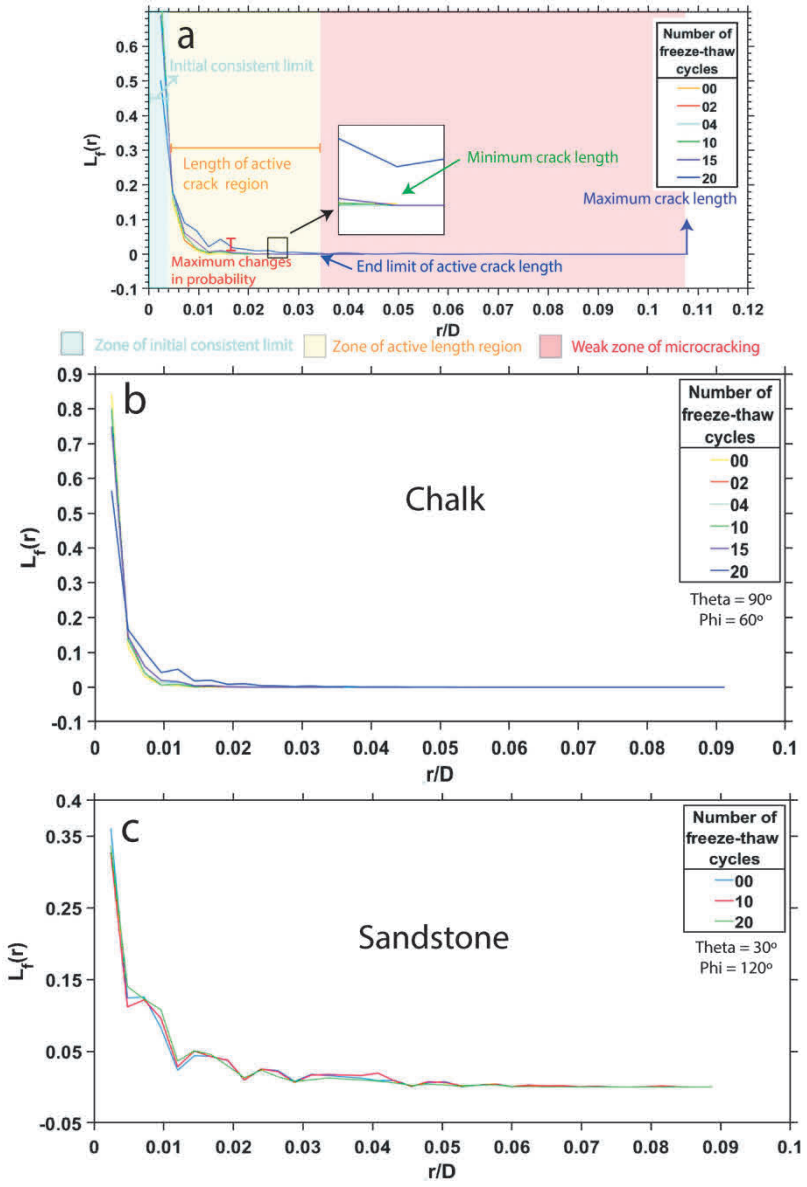

Fig. 7. (a) Classification plot of the parameters that describe the different segments of the lineal-path probability functions along a specific 3-D direction for different freeze–thaw cycles. The initial consistent limit denotes the small length of inherent flaws within the material which is not affected by the number of cycles. The active length region is the zone ahead of inherent flaws (crack tips) where noticeable change in probability—Lf(r)—occurred between initial and final cycles. The end limit of active crack region is marked by the condition when Lf(r) values of different cycles again merge with each other at near-zero values. The minimum and maximum crack length denote the length of the continuous fracture phase before the first cycle and after the final cycle. Lineal-path probability functions for chalk (b) and sandstone (c) in one of 49 predefined 3-D directions. 'r' is the distance between two points; 'D' is the diameter of the rock specimen. Note different range of y axis in both plots, and the maximum value of r/D on the x axis is not 1 (as in Figs. 5–6) but 0.1.

209x296mm (300 x 300 DPI)

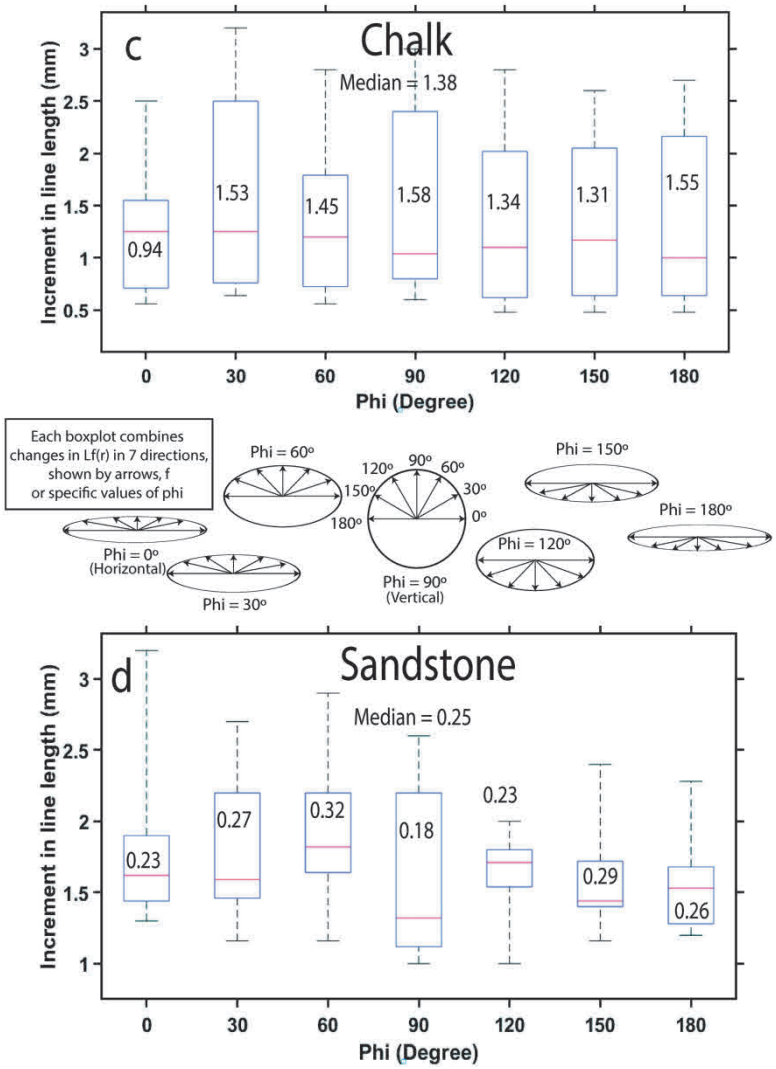

Fig. 8. Boxplots showing the increment in the probability values of Lf(r) and in the continuous line length (i.e., difference between maximum and minimum crack length) between 00 and 20 freeze–thaw cycles for 49 different (various combinations of θ and φ) 3-D directions for (a & c) chalk and (b & d) sandstone. Each φ (zenith angle) direction on the X-axis is weighted with seven θ (azimuth angle) directions, as shown by the arrows within the ellipses; thus each boxplot summarises changes in 7 directions. Horizontal red lines indicate median values. The average probabilistic increment in the zone of active crack and the average increment in the continuous line length in chalk and sandstone are 6 & 2% and 1.38 & 0.26 mm, respectively.

209x296mm (300 x 300 DPI)

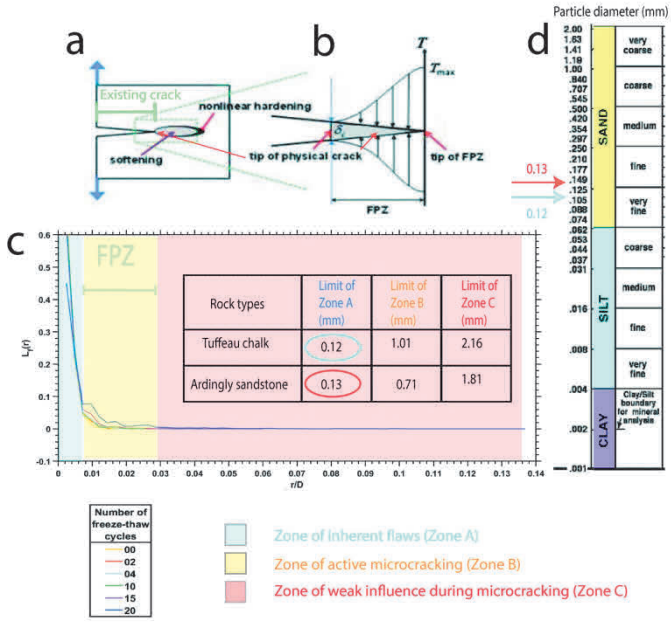

Fig. 9. Summary diagram integrating fracture mechanics concepts (a–b) with the microcracking zones identified in this study (c) relative to a sediment particle-size scale (d). (a) Illustrates schematically the development of the fracture process zone (FPZ) of an existing crack under tension. (b) Shows the mechanical changes across the FPZ; cohesive-zone traction (T) reaches a peak value, or cohesive strength (Tmax); ∂c is the cohesive-zone displacement. (c) Shows a graph of the linear-path function for one of the 49 directions simulated in the chalk specimen as a reference for the three newly classified microcracking zones, whose relative lengths (mm) are tabulated. Changes in Lf(r) are maximal in the FPZ, but negligible in the other two zones. The changes in the probability imply the development of existing microcracks in the FPZ. (d) The sediment particle-size scale relates the texture of the chalk and sandstone to the extent of the zone of inherent flaws (i.e., inherited microfabric). Sources: (a) and (b) from ref. (Im, Kim & Ban, 2013), and (d) from https://pubs.usgs.gov/of/2006/1195/htmldocs/nomenclature.htm.

209x296mm (300 x 300 DPI)